BRD9 Degradation Disrupts Ribosome Biogenesis in Multiple Myeloma

Keiji Kurata[1], Mehmet K. Samur[2], Priscilla Liow[3], Kenneth Wen[1], Leona Yamamoto[1], Jiye Liu[1], Eugenio Morelli[1], Annamaria Gulla[1,4], Yu-Tzu Tai[1], Jun Qi[3,5], Teru Hideshima[1], and Kenneth C. Anderson[1]

ABSTRACT

Purpose: BRD9 is a defining component of the noncanonical SWI/SNF complex, which regulates gene expression by controlling chromatin dynamics. Although recent studies have found an oncogenic role for BRD9 in multiple cancer types including multiple myeloma, its clinical significance and oncogenic mechanism have not yet been elucidated. Here, we sought to identify the clinical and biological impact of BRD9 in multiple myeloma, which may contribute to the development of novel therapeutic strategies.

Experimental Design: We performed integrated analyses of BRD9 *in vitro* and *in vivo* using multiple myeloma cell lines and primary multiple myeloma cells in established preclinical models, which identified the molecular functions of BRD9 contributing to multiple myeloma cell survival.

Results: We found that high BRD9 expression was a poor prognostic factor in multiple myeloma. Depleting *BRD9* by genetic (shRNA) and pharmacologic (dBRD9-A; proteolysis-targeting chimera; BRD9 degrader) approaches downregulated ribosome biogenesis genes, decreased the expression of the master regulator MYC, and disrupted the protein-synthesis maintenance machinery, thereby inhibiting multiple myeloma cell growth *in vitro* and *in vivo* in preclinical models. Importantly, we identified that the expression of ribosome biogenesis genes was associated with the disease progression and prognosis of patients with multiple myeloma. Our results suggest that BRD9 promotes gene expression by predominantly occupying the promoter regions of ribosome biogenesis genes and cooperating with BRD4 to enhance the transcriptional function of MYC.

Conclusions: Our study identifies and validates BRD9 as a novel therapeutic target in preclinical models of multiple myeloma, which provides the framework for the clinical evaluation of BRD9 degraders to improve patient outcome.

Introduction

The mammalian SWI/SNF complex (SWItch/sucrose nonfermentable) is a chromatin-remodeling complex, which modulates genomic architecture and DNA accessibility, thus controlling gene expression (1–4). Nearly 25% of all cancer samples harbor mutations in the genes encoding its subunits (5, 6). The mSWI/SNF complex consists of three subfamilies: canonical BAF (cBAF), polybromo-associated BAF (PBAF), and the recently identified noncanonical BAF (ncBAF), each of which possesses common and complex-specific subunits (7, 8).

BRD9 is a component of the ncBAF complex and is an oncogene in a variety of cancers (9). In SMARCB1-deficient malignant rhabdoid tumors (10) and synovial sarcoma with SS18–SSX fusion protein (11, 12), BRD9 promotes the survival of tumor cells, and its depletion suppresses tumor cell growth. Interestingly, unlike the cBAF and PBAF complexes, mutations in the ncBAF complex are not frequently reported in cancer (9). Instead, BRD9 expression tends to be increased by amplifying *BRD9* copy number. Although therapeutic strategies targeting BRD9 are being explored (9–17), the mechanism of BRD9 in tumorigenesis has not been fully delineated. A recent study showed that BRD9 degrader is a chemosensitizer in multiple myeloma (MM; ref. 17); however, the *in vivo* efficacy and precise molecular mechanism of action of BRD9 degradation-induced MM cell growth inhibition have not been examined. Moreover, the biological impact of BRD9 in patients with MM is still unclear.

Alterations in ribosome biogenesis and translational activity play a critical role in cancer initiation and progression (18, 19). Ribosome biogenesis promotes specific translation programs, independent of the genetic makeup of the cancer (19–21), and plays a central role in activating oncogenic downstream signaling in cancer cells (22). In fact, recent studies have evaluated the inhibition of ribosome biogenesis as a novel therapeutic approach (23–28).

Given BRD9's importance in multiple cancers, we assessed its significance and mechanism in MM, which is incurable and the second most common hematologic malignancy (29). We found that BRD9 depletion decreased ribosome biogenesis and protein synthesis by interrupting the formation of a transcription initiation complex, which impacted survival and validates BRD9 as a potential novel therapeutic target.

Materials and Methods

Cell lines

The L363, MM.1S, NCI-H929, RPMI8226, and U266 human MM cell lines, as well as the HEK293T human embryonic kidney cell line, were purchased from ATCC. MOLP-8 cells were purchased from

[1]Jerome Lipper Multiple Myeloma Center, LeBow Institute for Myeloma Therapeutics, Dana-Farber Cancer Institute, Harvard Medical School, Boston, Massachusetts. [2]Department of Biostatistics and Computational Biology, Dana-Farber Cancer Institute and Harvard School of Public Health, Boston, Massachusetts. [3]Department of Cancer Biology, Dana-Farber Cancer Institute, Boston, Massachusetts. [4]Candiolo Cancer Institute, FPO-IRCCS, Turin, Italy. [5]Department of Medicine, Harvard Medical School, Boston, Massachusetts.

Corresponding Authors: Keiji Kurata, Dana-Farber Cancer Institute, 450 Brookline Avenue, Boston, MA 02215. E-mail: keiji_kurata@dfci.harvard.edu; and Kenneth C. Anderson, kenneth_anderson@dfci.harvard.edu

Clin Cancer Res 2023;29:1807–21

doi: 10.1158/1078-0432.CCR-22-3668

Translational Relevance

BRD9 is a defining component of the noncanonical SWI/SNF complex and has recently received attention as a therapeutic target in several types of cancer, including multiple myeloma. However, the mechanism of BRD9 in tumorigenesis, as well as the *in vivo* efficacy and biological significance of its degradation, have not been fully delineated. Here, we validated that BRD9 depletion impairs multiple myeloma cell survival in the bone marrow microenvironment and *in vivo*. We found a novel function for BRD9 in promoting ribosome biogenesis in multiple myeloma. Conversely, BRD9 depletion impairs ncBAF localization to its genomic targets, thereby disrupting the ribosome biogenesis machinery. Because overexpression of BRD9 and activated ribosome biogenesis play critical roles in driving multiple myeloma tumorigenesis, our results provide the rationale for further evaluation of BRD9 degraders as novel therapeutic options in multiple myeloma.

DSMZ. The KMM-1, KMS-11, KMS-12 PE, KMS-21 BM, KMS-26, KMS-27, and KMS-34 cell lines were obtained from JCRB (National Institute of Health Sciences). OPM2 cells were provided by Dr. Naoki Hosen (Osaka University). The MM.1R cell line was obtained from Dr. Steven Rosen. All MM cell lines were cultured in 5% CO_2 at 37°C in RPMI1640 medium (Thermo Fisher Scientific) containing 10% FBS (Sigma-Aldrich), 2 mmol/L L-glutamine, 100 U/mL penicillin, and 100 mg/mL streptomycin (Invitrogen). HEK293T cells were cultured in DMEM (Thermo Fisher Scientific) containing 10% FBS, 100 U/mL penicillin, and 100 mg/mL streptomycin. Cell lines were used within 3 months after thawing. Mycoplasma contamination was checked for using the MycoAlert Mycoplasma Detection Kit (Lonza).

Primary patient MM cells and bone marrow stromal cells (BMSC)

According to the Declaration of Helsinki, primary patient MM cells were obtained from bone marrow aspirates of patients with MM with written informed consent. Mononuclear cells were separated using Ficoll–Paque PLUS (GE Healthcare Bio-Sciences). Primary MM cells were further purified by $CD138^+$ selection using anti-CD138 magnetic-activated cell separation microbeads (Miltenyi Biotec). $CD138^-$ mononuclear cells were used to establish long-term BMSCs. All experiments with patient samples were performed according to a protocol approved by the Institutional Review Board of the Dana-Farber Cancer Institute.

Cell viability assay

Viable cells were determined using MTT (Sigma-Aldrich), as described previously (30). Briefly, cultured cells (100 μL/well) were pulsed with 10 μL of MTT solution (5 mg/mL) in 96-well plates and incubated for another 4 hours. After mixing with 100 μL of isopropanol containing 0.04 N HCl, absorbance was measured at 570 nm, with 620 nm as a reference wavelength using a SpectraMax M3 microplate reader (Molecular Devices LLC). For primary MM cells, viable cells were determined using CellTiter-Glo Luminescent Cell Viability Assay (Promega), as described previously (30). Briefly, cultured cells (100 μL/well) were mixed with 100 μL of CellTiter- Glo reagent in 96-well opaque-walled plates and incubated for 10 minutes at room temperature. Luminescence was recorded using a SpectraMax M3 microplate reader (Molecular Devices LLC).

Cell-cycle analysis

As described previously (30), cells were fixed with 70% ethanol for 20 minutes at 4°C and washed with PBS twice. Cells were then incubated with 5 μg/mL RNase (Roche) in PBS for 30 minutes at 37°C and then suspended in PBS containing 10 μg/mL propidium iodide (Sigma-Aldrich). The stained cells were analyzed using flow cytometry (BD FACSFortessa; BD Biosciences), and the cell-cycle distribution was determined using the ModFit LT software (Verity Software House).

Apoptosis assay

Apoptotic cells were determined using FITC Annexin V Apoptosis Detection Kit I (BD Biosciences), as described previously (30). After washing with ice-cold PBS twice, cells were resuspended in 1× binding buffer (10 mmol/L Hepes-NaOH, pH 7.4, 140 mmol/L NaCl, 2.5 mmol/L $CaCl_2$), incubated with FITC-conjugated Annexin V for 15 minutes at room temperature, and then analyzed using flow cytometry (BD FACSFortessa; BD Biosciences).

qRT-PCR

Total RNA was isolated using the RNeasy Mini Kit (Qiagen). Complementary DNA was then synthesized from 1 mg of total RNA with oligo(dT) primers using the Superscript IV Master Mix (Thermo Fisher Scientific). qRT-PCR was carried out using Power SYBR Green PCR Master Mix (Thermo Fisher Scientific) and QuantStudio 6 Flex Real-Time PCR System (Applied Biosystems). The relative amount of each transcript was determined using the relative standard curve method. The values were normalized to invariant control GAPDH expression. Specific primers for each gene are listed in Supplementary Materials and Methods.

Immunoblotting

Cells were washed with PBS and lysed in RIPA buffer (Cell Signaling Technology) with PMSF (Cell Signaling Technology). The lysates were incubated for 30 minutes at 4°C and then centrifuged at 14,000 rpm for 10 minutes at 4°C; supernatants were used as whole-cell lysates. After protein concentration was determined using the Bio-Rad Protein Assay (Bio-Rad Laboratories), samples were mixed with 4× Laemmli SDS-Sample Buffer (Boston BioProducts Inc.), boiled at 95°C for 5 minutes, and separated by SDS-PAGE. Separated proteins were dry-blotted onto nitrocellulose iBlot Transfer Stacks in iBlot Gel Transfer Devices (Thermo Fisher Scientific) for 7 minutes. The membranes were blocked in TBS containing 0.1% (v/v) Tween 20 and 5% (w/v) nonfat dry milk for 1 hour at room temperature; immunoblots were then carried out using the antibodies described in Supplementary Materials and Methods and visualized using ECL Prime Western Blotting Detection Reagent (Cytiva). The membranes were re-probed after stripping off antibodies with OneMinute Plus Western Blot Stripping Buffer (GM Biosciences).

Co-immunoprecipitation (Co-IP) assay

Co-IP was performed using either the Pierce Co-Immunoprecipitation Kit (Thermo Fisher Scientific) or the nuclear complex Co-IP Kit (Active Motif), according to the manufacturer's instructions. A total of 1 mg of whole-cell lysate or 200 to 300 μg of nuclear extract was used for Co-IP with 1 to 2 μg of antibodies listed in Supplementary Materials and Methods. Protein G Agarose Columns (Active motif) were used to capture the nuclear protein/antibody complex.

Expression plasmids

Lentivirus packaging plasmids (psPAX2 and VSV-G) and pLKO-based expression plasmids were obtained from the Broad Institute. An

shRNA vector against luciferase (shLuc) was used as a negative control for sh-mediated knockdown experiments. The TRC clone ID and target sequence of each vector is described in Supplementary Materials and Methods. The TurboGFP-IRES-luciferase bicistronic expression vector (MSCV-TurboGFP-IRES-Luc) was generated as described previously (30).

Viral production and infection for overexpression and knockdown of specific proteins

As described previously (30), 1 day before transfection, 293T packaging cells were plated into 6-well plates at a density of 6×10^5 cells/well. Cells were cotransfected with 1 μg of expression plasmid, 1 μg of psPAX2, and 200 ng of VSV-G for lentivirus packaging, or with 1 μg of pMSCV, 1 μg of pMD-MLV, and 200 ng of VSV-G for retrovirus packaging, using TransIT-LT1 Transfection reagent (Mirus Bio) according to the manufacturer's instructions. One day after transfection, cells were refed with fresh medium containing 30% (v/v) FBS. After 24 hours, medium containing virus was harvested, passed through 0.45 μmol/L cellulose acetate membrane filters, and used fresh for infection. MM cells were spinocculated with viral supernatant in the presence of 8 μg/mL polybrene at $800 \times g$ for 30 minutes at room temperature and further infected in 5% CO_2 at 37°C for 5 hours. After 24 hours, lentivirus-infected cells were selected with puromycin dihydrochloride (Sigma-Aldrich) at 1 μg/mL for 2 days. For the generation of OPM2-TurboGFP-Luc, TurboGFP-Luc expressing cells were selected using a cell sorter (BD FACSAria III; BD Biosciences). The human MYC expression vector was constructed by amplifying MYC cDNA using PCR and inserting into the pLenti-DDK-P2A-Puro empty vector (OriGene Technologies, PS100092).

Nuclear staining and live-cell imaging

The stain was prepared by mixing 1 mL of PBS with 1 μL of Nuclear-ID green/red detection reagent (Enzo Life Sciences). Cells cultured in 6-well plates at 80% confluence were washed once with PBS. A mixture of 250 μL of stain mix and 250 μL of complete media was added to each plate. Plates were incubated at 37°C in a humidified incubator with 5% CO_2 for 15 minutes. Live-cell nucleolar images were captured using Leica THUNDER imager at 63× magnification. The numbers of nucleoli were counted in at least 100 cells in each sample. Experiments were repeated three times. Significance was determined using a *t* test and all error bars indicate SD.

Polysome profiling

Polysome profiling was performed as described previously (31). After pretreatment with DMSO or dBRD9-A (100 nmol/L) for 48 hours, cycloheximide (100 μg/mL) was added to OPM2 cells for 15 minutes before lysis to freeze ribosomes on mRNAs in the elongation phase. Approximately 1×10^7 cells were lysed in hypotonic buffer (5 mmol/L Tris-HCl pH 7.5, 1.5 mmol/L KCl, 2.5 mmol/L $MgCl_2$, 0.5% Triton X-100, 0.5% deoxycholate, 2 mmol/L DTT) containing 100 μg/mL cycloheximide, 0.2 U/mL RNase inhibitor, and proteinase inhibitor cocktail (Abcam) on ice for 20 minutes. Equal amounts of A_{260} absorbance from each sample were loaded onto a 10% to 50% sucrose gradient solution and centrifuged at 35,000 rpm for 2 hours. RNA absorbance of each fraction was monitored at 254 nm to detect ribosomal subunits.

Protein synthesis assay

After pretreatment with DMSO or dBRD9-A (100 nmol/L) for 72 hours, samples were further processed according to the manufacturer's instructions using Protein Synthesis Assay Kit (Cayman Chemical). Cells were then resuspended with OPP Working Solution for 30 minutes at 37°C, washed and stained with the 5 FAM-Azide Staining Solution, and analyzed by flow cytometry (BD FACSFortessa; BD Biosciences).

GEP analysis

Gene Expression Omnibus data sets [GSE39754 (32) and GSE6477 (33)] and the MM Research Foundation (MMRF) CoMMpass (ClinicalTrials.gov identifier: NCT01454297) data sets were used for gene expression analyses. The 220155_s_at and 284559 were used for BRD9 on Affymetrix Human Genome U133A Array or Human Exon 1.0 ST Array. Ribosome biogenesis signature was analyzed according to the expression of genes as defined by ribosome biogenesis (biological process ontology) in the Molecular Signature Database (MSigDB; https://www.gsea-msigdb.org/gsea/msigdb/). Violin plots and Kaplan–Meier curves are depicted using GraphPad Prism9 software. To analyze the activity of the ribosome biogenesis pathway in primary MM cells, we used RNA-sequencing (RNA-seq) data from 319 newly diagnosed patients with MM who were enrolled in the Intergroupe Francophone du Myélome (IFM)/DFCI 2009 study (34, 35) and analyzed with single-sample gene set enrichment analysis (ssGSEA; ref. 36).

Genome-wide CRISPR-knockout screening data analysis

DepMap (https://depmap.org/portal/) analysis of the dependency of a panel of tumor cell lines on individual genes was conducted using the most recent (January 2022) CRISPR (DepMap 21Q4 Public 21Q4+Score, Chronos) database.

Xenograft model

For the disseminated model, we intravenously injected 1×10^6 OPM2 TurboGFP-Luc cells into 6-week-old female NOD.Cg-Prkdc^{scid} Il2rg^{tm1Wjl}/SzJ (NSG) mice (Jackson Laboratory). Tumor burden was serially monitored by BLI using the IVIS Imaging System and Living Image Software (PerkinElmer). After tumor engraftment, the mice were randomly divided into two groups and then intraperitoneally treated with dBRD9-A at 50 mg/kg or vehicle (DMSO in 10% of hydroxypropyl-β-cyclodextrin) once a day for 3 weeks.

For the plasmacytoma model, we subcutaneously injected 5-week-old female NOD.CB17-Prkdc^{scid}/NCrCrl (NOD/SCID) mice (Charles River Laboratories) in the right flank with 5×10^6 OPM2 TurboGFP-Luc cells mixed with PBS and 50% Matrigel. The mice were serially imaged after inoculation. In parallel, tumor size was measured using an electronic caliper, and tumor volume was determined using the formula: $(\text{length} \times \text{width}^2) \times 2^{-1}$, where length is greater than width. After tumor engraftment was confirmed by BLI signal and tumor size measurement, the mice were randomly divided into two groups and then intraperitoneally treated with dBRD9-A at 50 mg/kg or vehicle once a day for 3 weeks, as described previously (11). Animal studies were performed under a protocol approved by the Dana-Farber Institutional Animal Care and Use Committee.

Quantification of nucleolar organizer regions by silver staining

The paraffin-embedded tumor slides from mice were deparaffinized in xylene, hydrated using a graded series of alcohol, and assessed for argyrophilic nuclear organizing regions (AgNOR) according to a modified protocol (37). Cells were fixed in 2% glutaraldehyde followed by postfixation in ethanol–acetic acid solution (3:1), stained using a 0.33% formic acid–33.3% silver nitrate solution in 0.66% gelatin, and then mounted on slides using SlowFade Diamond Antifade Mountant

(Invitrogen). AgNOR numbers in at least 100 cells on each slide were quantified at 100× magnification. Experiments were repeated three times.

IHC analysis

Subcutaneous tumors were excised and fixed in 4% paraformaldehyde overnight and stored in 70% ethanol. IHC staining was performed in iHisto Inc., using the antibodies described in Supplementary Materials and Methods.

RNA-seq and polysome-seq

Total RNA was extracted from OPM2 and H929 cells using the RNeasy Plus Mini Kit (Qiagen) after 24 hours of treatment with 100 nmol/L of dBRD9-A or DMSO, or after 48 hours of puromycin selection following shBRD9 or shLuc transduction in biological triplicate. For polysome-seq, all polysome (≥3 ribosomes) fractions were pooled, and total RNA was extracted from the same volume of each sample using TRizol Plus RNA Purification Kit (Thermo Fisher Scientific) in biological triplicate. Library preparation was performed in the Molecular Biology Core Facilities at the Dana-Farber Cancer Institute using Roche Kapa mRNA HyperPrep strand-specific sample preparation reagents from 200 ng of purified total RNA on a Beckman Coulter Biomek i7. The finished dsDNA libraries were quantified using the Qubit fluorometer and Agilent TapeStation 4200. Uniquely dual-indexed libraries were pooled in an equimolar ratio and shallowly sequenced on an Illumina MiSeq to evaluate library quality and pool balance. The final pool was sequenced on an Illumina NovaSeq 6000 with paired-end 100bp reads at the Dana-Farber Cancer Institute Molecular Biology Core Facilities. RNA-seq and polysome-seq data are in the Gene Expression Omnibus (GEO) database (GSE197487).

Chromatin immunoprecipitation (ChIP)-seq

For ChIP experiments, OPM2 cells were harvested following 6 or 24 hours of treatment with 100 nmol/L of dBRD9-A or DMSO in biological duplicate. ChIP experiments were performed using the SimpleChIP Enzymatic Chromatin IP Kit (Cell Signaling Technology) with minor modifications. Briefly, cells were cross-linked for 10 minutes with 1% formaldehyde at room temperature. This reaction was subsequently quenched with 125 mmol/L glycine for 5 minutes, and 5 to 10 million fixed cells were used per ChIP experiment. Chromatin from fixed cells was fragmented with Micrococcal nuclease for 20 minutes at 37°C followed by sonication with a Q700 Sonicator (Qsonica), and the solubilized chromatin was incubated with the indicated antibody (listed in Supplementary Materials and Methods) overnight at 4°C. For BRD9 ChIP and GLTSCR1 ChIP, spike-in normalization was performed using spike-in *Drosophila* chromatin (Active Motif) and spike-in antibody against *Drosophila*-specific histone H2Av (Active Motif), according to the manufacturer's instructions [ChIP-Rx (Reference exogenous normalized)]. Antibody–chromatin complexes were pulled down by incubation with protein G magnetic beads for 2 hours at 4°C, washed, and eluted. Immunoprecipitated DNA was treated with Proteinase K and purified.

Library preparation was performed in the Molecular Biology Core Facilities at the Dana-Farber Cancer Institute using Swift S2 Acel reagents on a Beckman Coulter Biomek i7 liquid handling platform from approximately 1 ng of DNA and 14 cycles of PCR amplification. Sequencing was performed on an Illumina NovaSeq6000 with paired-end 150 bp reads. The ChIP-seq data in this study have been deposited in the GEO database (GSE197486).

RNA-seq and ChIP-seq data analysis

RNA-seq fastq files were aligned to GRCh37/hg19 and normalized using STAR. Differential expression data were obtained using the DEseq algorithm. These analyses were all done through the Basepair analysis platform (http://www.basepair.io).

ChIP-seq analysis was performed using pipelines on the omics analysis platform Basepair (http://www.basepair.io). ChIP fastq files were trimmed to remove adapter and low-quality sequences using trim_galore and aligned to the UCSC genome assembly hg19 using Bowtie2. For spike-in normalized ChIP-seq experiments, reads were separately aligned to hg19 and dm3 using Bowtie2. Duplicate reads were removed using Picard Mark Duplicates. Peaks were detected using MACS2 using a P value cutoff of 10^{-5}. Peaks were annotated to genomic features (Promoter, Gene body, Intergenic) using custom scripts on the Basepair platform, based on the UCSC database for hg19. ChIP-seq data visualizations were generated using the EaSeq analysis software (38).

Statistical analysis

For statistical comparison, a two-tailed Student t test was performed between two groups, assuming a normal distribution. IC_{50} values were determined by nonlinear regression using GraphPad Prism9 software. Univariate and multivariate analyses of prognostic factors related to survival were performed using the Cox proportional hazards model. The log-rank test was carried out to assess the significance of survival differences using GraphPad Prism9 software. A value of $P < 0.05$ was considered statistically significant.

Data availability

RNA-seq and ChIP-seq data have been deposited in the GEO database under SuperSeries accession number GSE197492, which is comprised of GSE197486 and GSE197487.

Results

BRD9 loss-of-function reduces MM cell growth *in vitro* and in *vivo*

We first used publicly available data from the DepMap project to assess the correlation between BRD9 knockout (KO) and cancer cell growth (39). Across 971 cancer cell lines, when BRD9 is targeted with CRISPR-Cas9, MM cell lines collectively rank as the third most affected in terms of fitness, following the known BRD9-dependent cancers synovial sarcoma and malignant rhabdoid tumor (Supplementary Fig. S1A). Although this effect seems small, it suggests a dependence on BRD9 in a subset of MM cells. Similar analyses performed on other mSWI/SNF genes in MM cells further indicated that the cBAF, PBAF, and ncBAF complexes are functionally distinct (Supplementary Fig. S1B), as components of those subcomplexes had similar effect sizes on fitness.

We next investigated the gene expression of BRD9 in primary MM patient cells. We found that *BRD9* tended to be highly expressed in patient MM cells compared with normal plasma cells (GSE39754, $P = 0.045$; GSE6477, $P = 0.185$; **Fig. 1A**; Supplementary Fig. S1C) and that higher *BRD9* expression was associated with poor overall survival (GSE39754, $P = 0.049$; MMRF CoMMpass, $P < 0.001$; **Fig. 1B**; Supplementary Fig. S1D). Importantly, these results maintained significance in a multivariate analysis with other risk factors [MMRF CoMMpass, HR = 1.636; 95% confidence interval (CI), 1.105–2.421; $P = 0.014$; Supplementary Table S1].

We next examined the effects of pharmacologic downregulation of BRD9 in MM cells using dBRD9-A, a potent and selective BRD9 chemical degrader (11). We first confirmed the results of DepMap by using BRD9 shRNA in the MM cell lines OPM2, H929, and MM.1S (Supplementary Fig. S1E). Then we treated OPM2 and H929 cells with dBRD9-A, which significantly degraded BRD9 without affecting the expression of other BRD family members or the BAF chromatin remodeling complex ATPase subunits SMARCA2/4 (**Fig. 1C**; Supplementary Fig. S1F). dBRD9-A treatment for 5 days inhibited growth in a panel of MM cell lines, with an IC_{50} of 10 to 100 nmol/L (**Fig. 1D**). Several cell lines were found to be less-sensitive and/or resistant to dBRD9-A, but this was not correlated to BRD9 expression level ($r = -0.113$; $P = 0.655$; Supplementary Data S1). OPM2 and H929 were selected for use in subsequent studies, as they exhibited medium-high sensitivity to dBRD9-A. In addition, dBRD9-A treatment of patients' MM samples resulted in a 40% to 60% reduction in cell viability, with minimal effects on the normal components of the bone marrow (**Fig. 1E** and **F**; Supplementary Fig. S1G). In contrast, dBRD9-A did not affect the viability of peripheral blood mononuclear cells (PBMC) from healthy volunteers (Supplementary Fig. S1H), suggesting a favorable therapeutic index.

We next examined the molecular mechanism whereby dBRD9-A triggers MM cell growth inhibition. In 96-hour cultures, dBRD9-A induced G_1 cell-cycle arrest in both OPM2 and H929 cells in a time-dependent manner (**Fig. 1G**; Supplementary Fig. S1I). dBRD9-A also triggered apoptosis after 96 hours, evidenced by annexin V staining (**Fig. 1H**; Supplementary Fig. S1J). Immunoblotting analyses further confirmed dose-dependent activation of apoptotic signaling, associated with the cleavage of caspases-8, -9, -3, and PARP (**Fig. 1I**). Taken together, these results indicate that dBRD9-A causes cell-cycle arrest followed by apoptosis.

BMSCs and soluble factors, including IL6 and IGF-1, promote MM cell growth, survival, and drug resistance (40, 41). We therefore examined whether dBRD9-A still maintains its cytotoxic effect against MM cells in the presence of exogenous IL6 or IGF-1 and found that neither inhibited dBRD9-A-induced cytotoxicity in OPM2 or H929 cell lines after 5 days of treatment (**Fig. 1J**). Furthermore, we cultured OPM2 and H929 cells with and without BMSCs and found that dBRD9-A still significantly inhibited BrdUrd uptake after 5 days of treatment (**Fig. 1K**).

We next examined the effect of dBRD9-A *in vivo* using a xenograft murine model of human MM. We first engineered OPM2 cells to express luciferase (Luc) and then intravenously injected these cells into NSG mice. After systemic engraftment, we randomized mice to receive either dBRD9-A (50 mg/kg, once a day) or vehicle via intraperitoneal injection for 21 days, with equivalent bioluminescence imaging (BLI) intensity in each group ($n = 8$ for each group; Supplementary Fig. S1K). dBRD9-A treatment significantly inhibited OPM2 tumor growth, evidenced by BLI, and improved overall survival when compared with the vehicle-treated control group (**Fig. 1L** and **M**; Supplementary Fig. S1L), without causing significant body weight loss (Supplementary Fig. S1M). To evaluate dBRD9-A in a plasmacytoma model, we subcutaneously injected OPM2 TurboGFP-Luc cells into NOD/SCID mice and then treated them with dBRD9-A (50 mg/kg, once a day) or vehicle control after tumor engraftment. As in our intravenous model, dBRD9-A treatment for 21 days also significantly inhibited tumor growth, evidenced both by BLI and tumor size measurement (Supplementary Fig. S1N–S1P), and improved overall survival when compared with the vehicle-treated control group (Supplementary Fig. S1Q).

Altogether, these results show that BRD9 expression is positively correlated with MM cell growth and that the pharmacological degrader dBRD9-A is effective at reducing MM cell growth without harming healthy cells and is well tolerated *in vivo*.

Induction of synergistic MM cell growth inhibition by BRD9 degradation

BRD9 degraders are more effective than small molecule inhibitors (11, 42) and are promising novel agents for clinical application (43). However, combination therapy with proteasome inhibitors and immunomodulatory drugs (IMiD) is the standard treatment option for MM, and these drugs alter proteolysis efficiency and targeting, which affects BRD9 degradation. Therefore, we sought to find rational candidates for combination therapy with dBRD9-A (Supplementary Fig. S2A). Several small molecules, including the CDK4/6 inhibitor palbociclib, activate proteasome activity (44–46). Indeed, palbociclib, as well as the conventional myeloma agents melphalan and dexamethasone, demonstrated synergistic growth inhibition with dBRD9-A in OPM2 and H929 cells (Supplementary Fig. S2H). In particular, dexamethasone induced a strong synergistic effect in OPM2, H929, and MM.1S cells, but not in MM.1R cells, consistent with a previous report that BRD9 restricts binding of glucocorticoid receptors (47).

BRD9 expression is positively correlated with ribosome biogenesis

Although our results showed that BRD9 depletion had a growth inhibitory effect on MM cells, the *in vitro* sensitivity of MM cell lines to dBRD9-A varied widely (**Fig. 1D**). Our initial screening across cell lines did not show a correlation between dBRD9-A susceptibility and BRD9 expression level ($r = -0.113$; $P = 0.655$; Supplementary Data S1), the presence of mutations in subunits of the mSWI/SNF complex (likely due to their low frequency; ref. 48), or the genetic subset of MM (Supplementary Fig. S2B). Therefore, to find the mediators of susceptibility to BRD9 depletion, we analyzed the correlation between the expression level of each gene and either the IC_{50} of dBRD9-A in our tested cell lines or the genetic perturbation value obtained by DepMap (**Fig. 2A**; ref. 39). Next, we divided the genes into two groups, those with a positive versus negative correlation, and then performed GSEA using the Kyoto Encyclopedia of Genes and Genomes (KEGG) Pathways (49) and Reactome Pathways (50) separately on each group. For the positively and negatively correlated genes, respectively, we found that 38 and 65 pathways were enriched in the dBRD9-A treatment group, whereas 234 and 28 pathways were enriched in the CRISPR-Cas9 KO treatment group (**Fig. 2B**; Supplementary Fig. S2C). Among the pathways shared by dBRD9-A and CRISPR-Cas9 KO were the ribosome, translation initiation and elongation, and rRNA processing pathways. Those pathways were in the negative correlation group (**Fig. 2C**), suggesting that BRD9 depletion–sensitive cell lines had higher ribosome biogenesis and translational activity.

Importantly, ribosome biogenesis genes (as defined by Gene Ontology) were highly expressed in patient MM cells compared with normal plasma cells (GSE39754, $P = 0.032$; GSE6477, $P < 0.001$; **Fig. 2D**; Supplementary Fig. S2D). Moreover, higher expression of ribosome biogenesis genes was associated with poor overall survival (GSE39754, $P = 0.031$; MMRF CoMMpass, $P < 0.001$; **Fig. 2E**; Supplementary Fig. S2E). On the other hand, there was no clear correlation between these ribosome biogenesis signatures and genetic background (Supplementary Fig. S2F). Taken together, these data demonstrate that enhanced ribosome biogenesis activity in MM is positively correlated with poor prognosis and BRD9 expression.

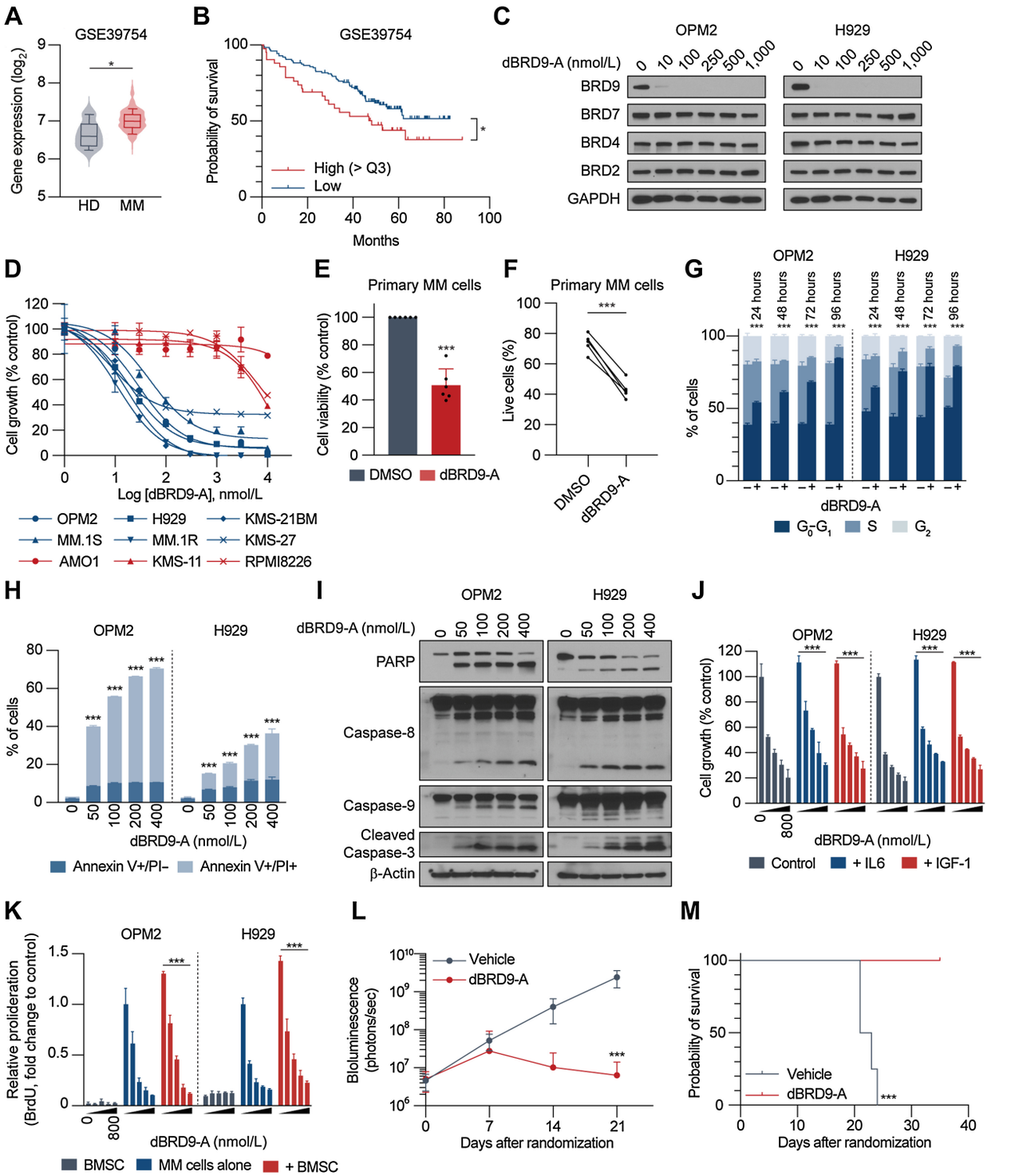

Figure 1.

Clinical impact and biological significance of BRD9 in multiple myeloma (MM) *in vitro* and *in vivo*. **A,** Comparative GEP analysis of *BRD9* expression between normal plasma cells and MM cells (GSE39754). **B,** Overall survival relative to *BRD9* expression in patients with newly diagnosed MM (GSE39754). **C,** Immunoblot analysis for BRD9, BRD7, BRD4, and BRD2 using GAPDH as a loading control after treatment with dBRD9-A for 24 hours at the indicated doses in OPM2 and H929 cells. **D,** MM cell lines were cultured with the indicated concentrations of dBRD9-A for 5 days. Viable cells were determined by MTT assay. **E,** CD138$^+$ primary MM cells separated from the BMMCs of 6 patients with MM were treated with or without dBRD9-A (1 μmol/L) for 3 days. The cell viability was assessed by CellTiter-Glo assay. **F,** BMMCs from patients with MM were cultured with or without dBRD9-A (1 μmol/L) for 48 hours and analyzed using multichannel flow cytometry. Viability of CD138-positive MM cells and CD138-negative normal BM stromal cells was determined by Annexin V and propidium iodide (PI) staining. (*Continued on the following page.*)

BRD9 depletion downregulates ribosome biogenesis

With a positive correlation between BRD9 expression and ribosome biogenesis established, we next sought to confirm the inverse: that BRD9 depletion would result in less biogenesis. After dBRD9-A application or BRD9 knockdown using shRNA, a total of 766 or 1,413 genes were upregulated, whereas 597 or 1,436 genes were downregulated, respectively, compared with control cells ($P_{adj} < 0.05$; Supplementary Data S2), and ribosome biogenesis and rRNA processing were the pathways most significantly downregulated in both experimental settings (**Fig. 3A–C**; Supplementary Fig. S3A and S3B). Furthermore, by overlapping differentially expressed genes, GSEA listed ribosome biogenesis and rRNA processing at the top of the list, using DAVID Bioinformatics Resources (refs. 51, 52; **Fig. 3A**). Importantly, gene sets involved in translation were also markedly downregulated (Supplementary Fig. S3C). qRT-PCR confirmed reduced mRNA expression of *MYC* and ribosome biogenesis genes after dBRD9-A treatment and after *BRD9* knockdown in OPM2 and H929 cells (**Fig. 3D** and **E**; Supplementary Fig. S3D–S3E). Furthermore, we observed that the expression of representative proteins (i.e., RRS1, PES1, and BOP1) was also consistently decreased by both dBRD9-A treatment and *BRD9* knockdown in OPM2 and H929 cells (**Fig. 3F** and **G**; Supplementary Fig. S3F–S3G). These results were further confirmed in primary MM patient cells (**Fig. 3H** and **I**) and by IHC analysis in tumor resected from dBRD9-A–treated xenograft mice (**Fig. 3J**). Taken together, these results suggest that MYC and ribosome biogenesis genes/proteins are downstream targets of BRD9.

Indeed, we observed a significant decrease in 47S pre-rRNA levels after treatment with dBRD9-A in OPM2 and H929 cells (**Fig. 4A**), and in patient samples, a decrease in 47S pre-rRNA, 18S, 5.8S, and 28S rRNA (**Fig. 4B**), consistent with downregulated transcription of RNA polymerase I (Supplementary Data S3). In contrast, 5S rRNA, regulated by RNA polymerase III, was not altered by dBRD9-A treatment. We also observed a significant reduction in nucleolar number upon dBRD9-A treatment (**Fig. 4C**). Polysome profiling of cytosolic extracts from OPM2 cells treated with dBRD9-A showed significantly fewer ribosomal subunits and actively translating polysomes compared with DMSO-treated controls (**Fig. 4D**). Furthermore, we sequenced the mRNA associated with polysomes (polysome-seq) and found no marked translation preference compared with the total RNA-seq results. However, GSEA revealed a decrease in the expression of pathways associated with translation, DNA replication, and ribosome biogenesis (**Fig. 4E**; Supplementary Data S3). Consistently, the synthesis of new protein was significantly reduced by BRD9 depletion (**Fig. 4F**). Furthermore, we performed AgNOR staining on tumors harvested from our murine xenograft model and found that dBRD9-A treatment induced a significant reduction of AgNOR counts *in vivo* (**Fig. 4G**).

BRD9 occupies and activates ribosome biogenesis genes

To understand how the BRD9-containing complex regulates the expression of ribosome biogenesis genes, we performed ChIP-seq and found that BRD9 preferentially binds gene promoters (47.7%) and distal intragenic regions (39.4%; **Fig. 5A**). Spike-in normalized BRD9 ChIP-seq (ChIP-Rx) demonstrated a significant loss of BRD9 binding across the genome after a 6-hour treatment with dBRD9-A (**Fig. 5B**). Additional ChIP-seq analyses of RNA polymerase II (RNAPII) and H3K27Ac further demonstrated that BRD9 binds virtually all active gene promoters and enhancer elements (**Fig. 5C**, shown is *MYC* as a representative example; Supplementary Fig. S4A). In addition, many of the genes downregulated by dBRD9-A had BRD9 occupancy at their promoters compared with other genes (**Fig. 5D**; Supplementary Fig. S4B). Importantly, GSEA using genes with BRD9 signals in their promoter regions were enriched for ribosome biogenesis and rRNA processing and were downregulated by dBRD9-A treatment (**Fig. 5E**). These results indicate that BRD9 directly regulates the expression of ribosome biogenesis genes, which can be partially blocked by pharmacologic depletion of BRD9.

BRD9 interacts with BRD4 to regulate transcription

Because BRD9 is an important component that defines ncBAF, we hypothesized that BRD9 depletion could disrupt proper ncBAF complex assembly. However, we observed that GLTSCR1, another ncBAF-specific component, still formed a complex even after complete BRD9 depletion by dBRD9-A (**Fig. 5F**; Supplementary Fig. S4C). However, without BRD9, there was a significant loss of GLTSCR1 binding across the genome, indicating BRD9 is needed for the binding of chromatin (**Fig. 5G**).

GLTSCR1 interacts with BRD4 to regulate the transcriptional elongation of target genes (53–55). BRD9 also interacts with the acetylated form of BRD4 in a bromodomain-dependent fashion in an embryonic stem cell model (56). Therefore, we hypothesized that the binding of BRD9 to the acetylated form of BRD4 stabilizes the binding of BRD4 to the ncBAF complex via GLTSCR1. Indeed, BRD9 Co-IP not only with BRD4, but also with the positive transcription elongation factor (P-TEFb; CDK9 and CCNT1), RNAPII, and MYC in MM cells (**Fig. 5H**; Supplementary Fig. S4D). The interaction between BRD9 and BRD4 was enhanced by histone deacetylase inhibitor (suberoylanilide hydroxamic acid, SAHA), which preserves acetylation on histones and nonhistone proteins (**Fig. 5I**; Supplementary Fig. S4E). On the other hand, BRD9 depletion attenuated the interaction between GLSTCR1 and BRD4 (**Fig. 5J**; Supplementary Fig. S4F).

To examine whether BRD9 depletion alters transcription initiation, we further assessed RNAPII phosphorylation at Ser5 and Ser2. Typically, Ser5p predominates at initiation, then Ser2P increases during elongation. In OPM2 and H929 cells treated with dBRD9-A, we found reduced phosphorylation at both Ser5 and Ser2. There was no change in the expression of negative elongation factor (NELFe), which represses elongation, or in CDK9 and CCNT1, which phosphorylate RNAPII (**Fig. 5K**; Supplementary Fig. S4G). Taken together, these results suggest that BRD9 interacts

(*Continued.*) The percentage of viable MM cells from 5 different patients is shown. **G,** OPM2 and H929 cells were incubated with dBRD9-A (100 nmol/L) for the indicated hours. Cells were fixed, stained with PI, and analyzed for cell-cycle distribution using flow cytometry. **H,** OPM2 and H929 cells were incubated with dBRD9-A at the indicated doses for 96 hours. Cells were stained with Annexin V and PI, and analyzed for apoptosis using flow cytometry. **I,** OPM2 and H929 cells were cultured with dBRD9-A at the indicated doses for 96 hours. Whole-cell lysates were subjected to immunoblotting using indicated antibodies. **J,** Serum-starved OPM2 and H929 cells were treated with dBRD9-A (100, 200, 400, and 800 nmol/L) for 5 days in the presence of IL6 (10 ng/mL) or IGF-1 (50 ng/mL). The cell growth relative to untreated control was assessed by MTT assay. **K,** OPM2 and H929 cells were cultured with dBRD9-A (100, 200, 400, and 800 nmol/L) for 5 days in the presence or absence of BMSCs. The cell proliferation relative to untreated control was assessed by BrdUrd uptake. **L,** Tumor burden was serially evaluated by bioluminescence imaging ($n = 8$ mice per group). **M,** Kaplan–Meier curves showing the survival of dBRD9-A–treated mice or vehicle control mice. Data represent mean ± SD of triplicate cultures (**D**, **G**, **H**, **K**). HD, healthy donor. *, $P < 0.05$; **, $P < 0.01$; ***, $P < 0.001$.

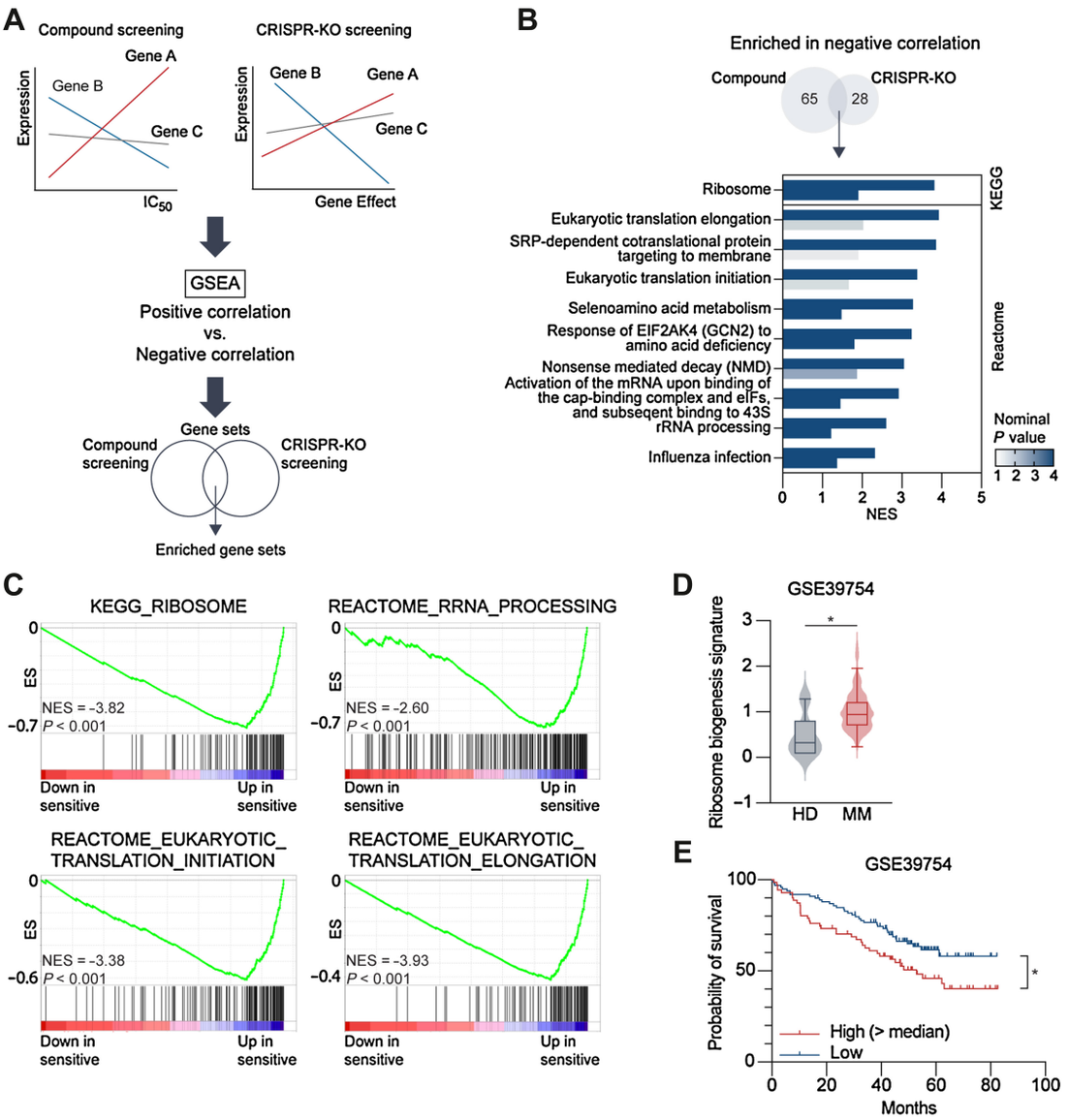

Figure 2.

Ribosome biogenesis and translation signatures are upregulated in BRD9 depletion–sensitive MM cell lines. **A,** Schematic diagram of genetic screening to identify the mediators for susceptibility to BRD9 depletion. The correlation between expression levels of each gene and the IC_{50} of dBRD9-A or gene perturbation values obtained by CRISPR-Cas9 KO screening was calculated for MM cells. Each gene was divided into two groups with positive and negative correlations to BRD9 depletion, and GSEA was performed. **B,** Venn diagram overlaps of enriched negatively correlated genes by compound (dBRD9-A) and CRISPR-Cas9–based screening (top). Bar graphs showing the significantly upregulated genes in BRD9 depletion–sensitive MM cells determined by querying the KEGG and reactome pathways (bottom). **C,** GSEA plots for ribosome, translation initiation and elongation, and rRNA processing. **D,** Comparative GEP analysis of ribosome biogenesis signature between normal plasma cells and MM cells (GSE39754, $n = 170$), summarized by boxplots and violin distributions. **E,** Overall survival relative to ribosome biogenesis signature in patients with newly diagnosed MM (GSE39754). FDR Q-val, false discovery rate Q-value; NES, normalized enrichment score; NOM *P*-val, nominal *P*-value. *, $P < 0.05$.

with the acetylated form of BRD4, stabilizing its binding to the ncBAF complex and thereby supporting the initiation of transcription of target genes.

BRD9 cooperates with BRD4 and MYC to promote ribosome biogenesis gene expression

Because we demonstrated that BRD9 interacts with BRD4 and MYC, we hypothesized that the expression of ribosome biogenesis genes is, at least in part, regulated by the interaction of BRD9 with BRD4 and/or MYC. ChIP-seq analysis demonstrated that BRD9-bound sites significantly overlapped with the ChIP peaks of BRD4, MYC, and RNAPII (**Fig. 6A**). Importantly, they colocalized to the promoter regions of all ribosome biosynthesis genes, as represented by RRP9 and NOP16 (**Fig. 6B** and **C**). ChIP-Rx showed that, as expected, the MYC signal was reduced by 24-hour treatment with dBRD9-A, but interestingly, the BRD4

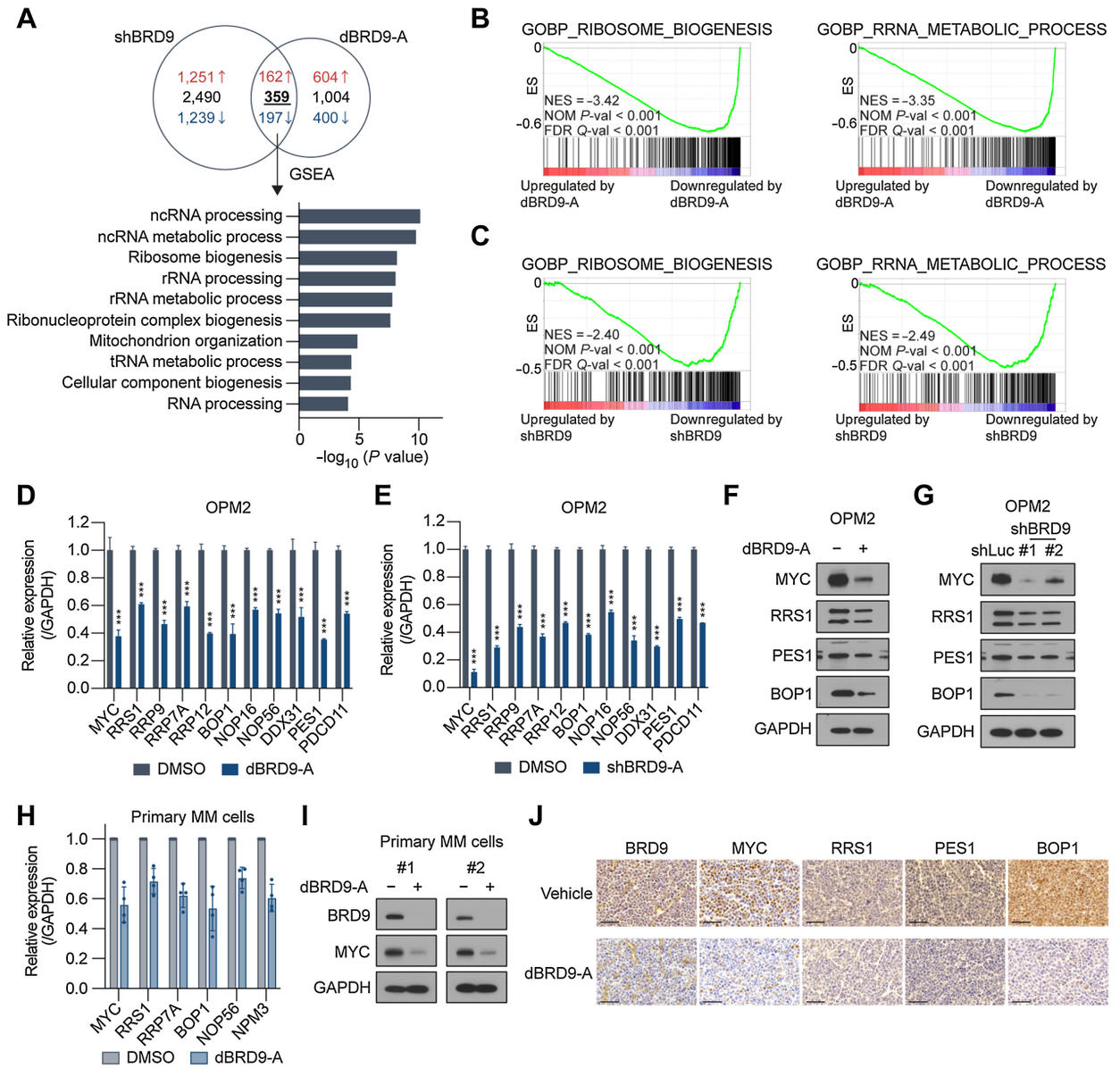

Figure 3.

Inhibition or knockdown of BRD9 downregulates expression of ribosome biogenesis genes. **A,** Venn diagram overlaps of genes differentially expressed by dBRD9-A and shBRD9 (top). Bar graphs showing the top 10 gene ontology enrichment results (bottom). **B** and **C,** GSEA plots for ribosome biogenesis and rRNA metabolic process after treatment with dBRD9-A (**B**) and BRD9 knockdown (**C**). **D** and **E,** Expression levels of representative ribosome biogenesis genes were assessed by qRT-PCR after treatment with 100 nmol/L of dBRD9-A or DMSO control for 24 hours (**D**) or transduction of shBRD9 or shLuc (**E**) in OPM2 cells. Data are normalized against the housekeeping control gene GAPDH. The expression relative to DMSO or shLuc are shown as mean ± SD of triplicate samples. **F** and **G,** Immunoblot analysis for ribosome biogenesis proteins after treatment with or without dBRD9-A (100 nmol/L) for 24 hours (**F**), or transduction of shBRD9 or shLuc (**G**) in OPM2 cells. **H** and **I,** $CD138^+$ primary MM cells separated from the BMMCs of 4 patients with MM were treated with or without dBRD9-A (100 nmol/L) for 24 hours, and the representative ribosome biogenesis mRNA level was measured by qRT-PCR (**H**) or BRD9 and MYC expression was assessed by immunoblotting (**I**). **J,** IHC analysis for BRD9, MYC, RRS1, PES1, and BOP1 in the subcutaneous tumor samples from the OPM2 TurboGFP-Luc–injected mice treated with dBRD9-A or vehicle control. Scale bars, 50 μmol/L. Data are representative of three independent tumors per treatment group. FDR Q-val, false discovery rate Q-value; NES, normalized enrichment score; NOM *P*-val, nominal *P*-value. ***, $P < 0.001$.

and RNAPII signals were unaltered (**Fig. 6D**), suggesting that BRD9 is not involved in the recruitment of BRD4 or RNAPII to genomic regions. Notably, most of the genes downregulated by dBRD9-A (97.8%) were co-occupied by BRD9, BRD4, and MYC in the TSS (**Fig. 6E**; Supplementary Fig. S5A). Downregulated genes had greater occupancy of MYC around the TSS compared with other BRD9, BRD4, and MYC co-occupied genes that were not downregulated by dBRD9-A (Supplementary Fig. S5B).

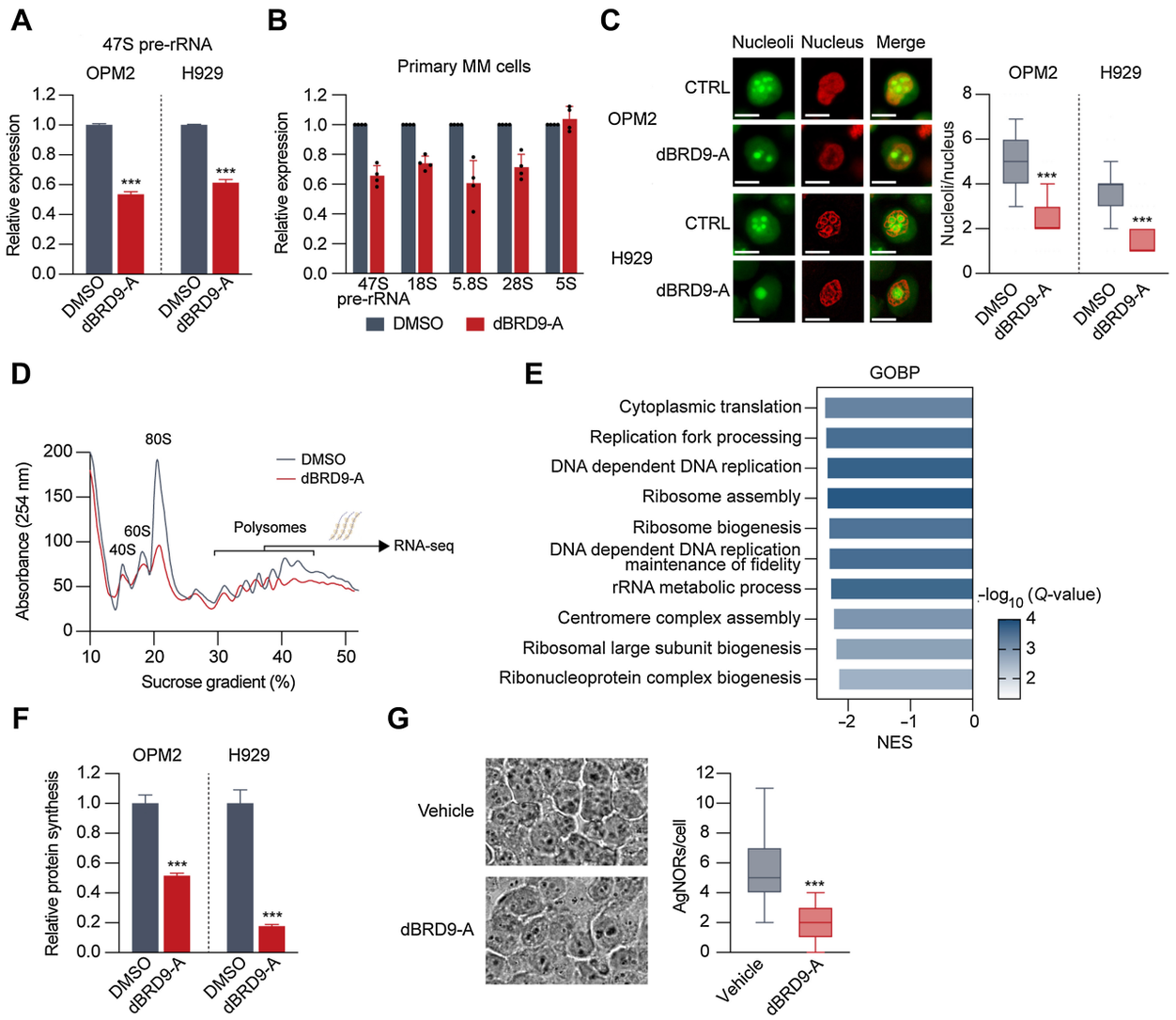

Figure 4.

BRD9 depletion decreases ribosome biogenesis activity. **A,** Expression level of 47S pre-rRNA was assessed by qRT-PCR after treatment with or without dBRD9-A (100 nmol/L) for 48 hours. **B,** CD138^{+} primary MM cells separated from the BMMCs of 4 patients with MM (using CD138-magnetic–activated cell separation beads) were treated with or without dBRD9-A (100 nmol/L) for 48 hours, and the rRNA levels were measured by qRT-PCR. **C,** OPM2 and H929 cells were treated with or without dBRD9-A (100 nmol/L) for 48 hours and then assessed for the number of nucleoli per nucleus. Representative photomicrographs are presented (left). Scale bars, 10 μmol/L. The accompanying bar graphs present the mean ± SD nucleoli/nucleus number (right). **D** and **E,** OPM2 cells were treated with or without dBRD9-A (100 nmol/L) for 48 hours, and cytosolic extracts from cells were loaded onto a 10% to 50% sucrose gradient and fractionated with recording UV (254 nm) monitoring. 40S, 60S, 80S, and polysomes represent small and large ribosomal subunits, monosomes, and multiple ribosomes per mRNA (**D**). Polysome-seq was performed on RNA extracted from pooled polysome (≥3 ribosomes) fractions. Bar plots showing the top 10 downregulated Gene Ontology pathways (Biologic Process, MSigDB; **E**). **F,** OPM2 and H929 cells were treated with or without dBRD9-A (100 nmol/L) for 72 hours, and protein synthesis was then assessed using flow cytometry. **G,** AgNOR staining in the subcutaneous tumor samples from the OPM2 TurboGFP-Luc–injected mice treated with dBRD9-A or vehicle control. Representative images are presented (left). The accompanying bar graphs present the mean ± SD of AgNOR number per cell (right). ***, $P < 0.001$.

Furthermore, we found that the genes co-occupied in the promoter regions were remarkably enriched for ribosome biogenesis (**Fig. 6F**).

Because MYC is the master regulator of ribosome biogenesis (57), we questioned whether the effect of dBRD9-A is mediated by MYC. We examined whether exogenous overexpression of MYC rescues the effect of dBRD9-A in MM cells. We used OPM2 and H929 cells stably expressing either exogenous Flag-tagged MYC or empty vector as a control. Treatment with dBRD9-A downregulated endogenous MYC mRNA and protein, and had no effect on exogenous MYC (**Fig. 6G** and **H**; Supplementary Fig. S5C and S5D). Alone, MYC overexpression did not induce further ribosome biogenesis gene expression except for the 47S pre-rRNA (**Fig. 6H**; Supplementary Fig. S5D). After dBRD9-A treatment, external MYC partially rescued ribosome biogenesis gene expression and cellular activity (**Fig. 6H** and **I**; Supplementary Fig. S5D and S5E), suggesting that BRD9 regulates the expression of ribosome biogenesis genes at least partly through the recruitment of MYC. Consistent with this result, RNA-seq analyses showed that

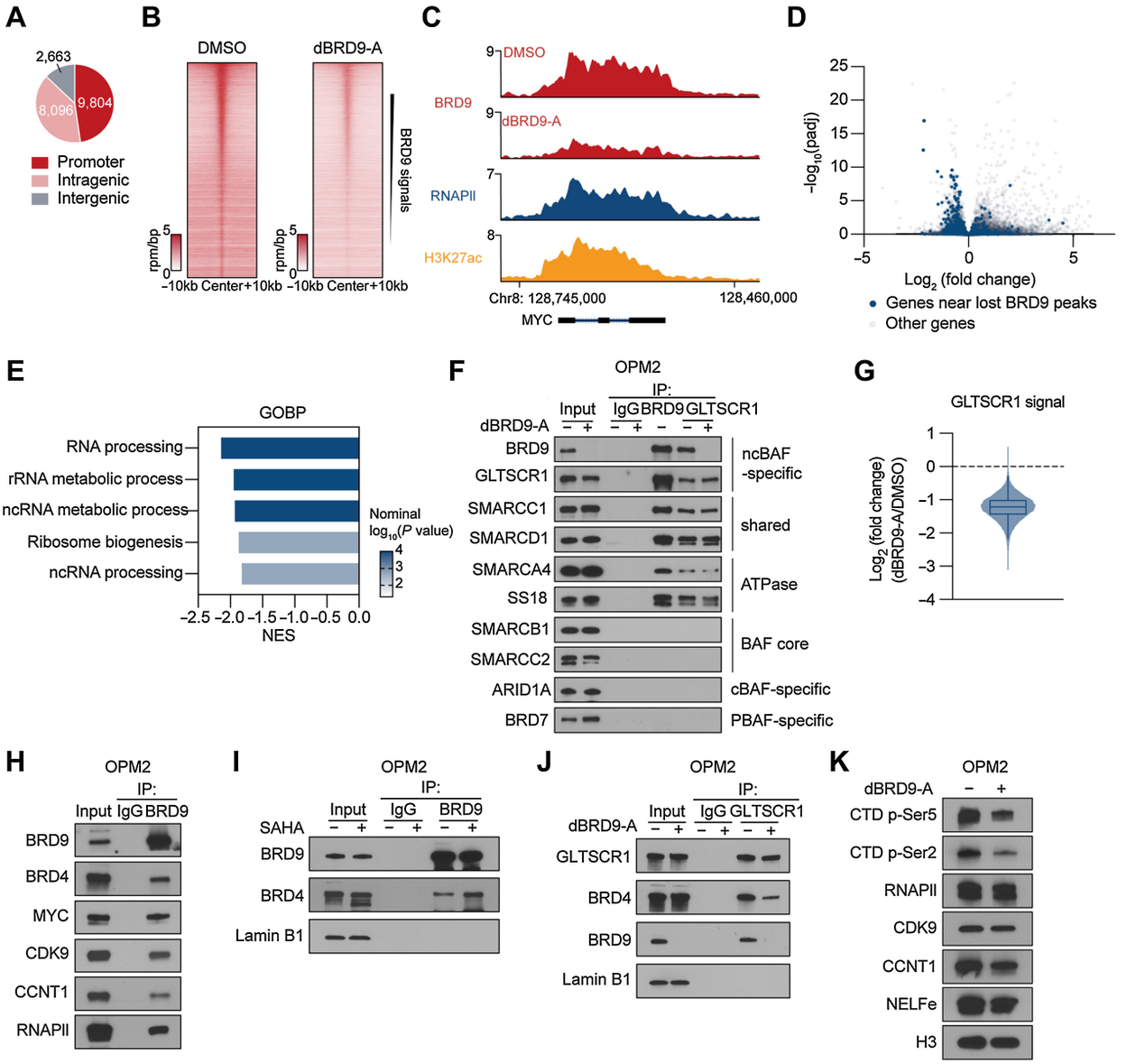

Figure 5.

BRD9 is required for chromatin binding of the ncBAF complex and regulates transcription. **A,** Pie charts representing the distribution of BRD9 binding sites in MM cells. **B,** Tornado plots representing BRD9 ChIP-Rx signal in dBRD9-A- (100 nmol/L, 6 hours) or DMSO-treated OPM2 cells. **C,** Representative gene tracks showing BRD9 ChIP-seq occupancy at the indicated genomic loci in dBRD9-A- or DMSO-treated cells. Also shown are RNAPII and H3K27Ac ChIP-seq signal in untreated cells. **D,** Differential analysis volcano plot of RNA-seq in OPM2 and H929 cells with dBRD9-A treatment (24 hours). Blue dots indicate genes with a TSS within 50 kb of a BRD9 signal lost site. **E,** The top five gene ontologies of GSEA in differentially expressed genes with BRD9 ChIP signals. **F,** OPM2 cells were treated with or without dBRD9-A (100 nmol/L) for 24 hours and harvested. Nuclear extracts were then immunoprecipitated with anti-BRD9 or anti-GLTSCR1 and subjected to immunoblot analysis with indicated antibodies. **G,** Violin plot representing changes in GLTSCR1 occupancy at GLTSCR1 peak regions in ChIP-Rx experiments of dBRD9-A (100 nmol/L)-treated OPM2 cells following 24 hours treatment. **H,** Nuclear extracts from OPM2 cells were immunoprecipitated with anti-BRD9 and subjected to immunoblot analysis with indicated antibodies. **I** and **J,** OPM2 cells were treated with DMSO or SAHA (3 μmol/L, 16 hours; **I**) and dBRD9-A (100 nmol/L, 24 hours; **J**). Nuclear extracts were then immunoprecipitated with anti-BRD9 (**I**) or anti-GLTSCR1 (**J**) and subjected to immunoblot analysis with indicated antibodies. **K,** OPM2 cells were treated with dBRD9-A (100 nmol/L) for 24 hours. Nuclear extracts were subjected to immunoblot analysis with indicated antibodies.

BRD9 depletion reduced the expression of MYC target genes (**Fig. 6J**; Supplementary Fig. S5F).

In summary, BRD9 preferentially colocalizes with BRD4 and MYC in the promoter region of ribosomal biogenesis genes and at least partially supports the transcriptional function of MYC, thereby promoting the expression of target genes. Pharmacologic or genetic loss of BRD9 disrupts ribosome biogenesis, leading to impaired translational function and cell death in MM cells (**Fig. 6K**).

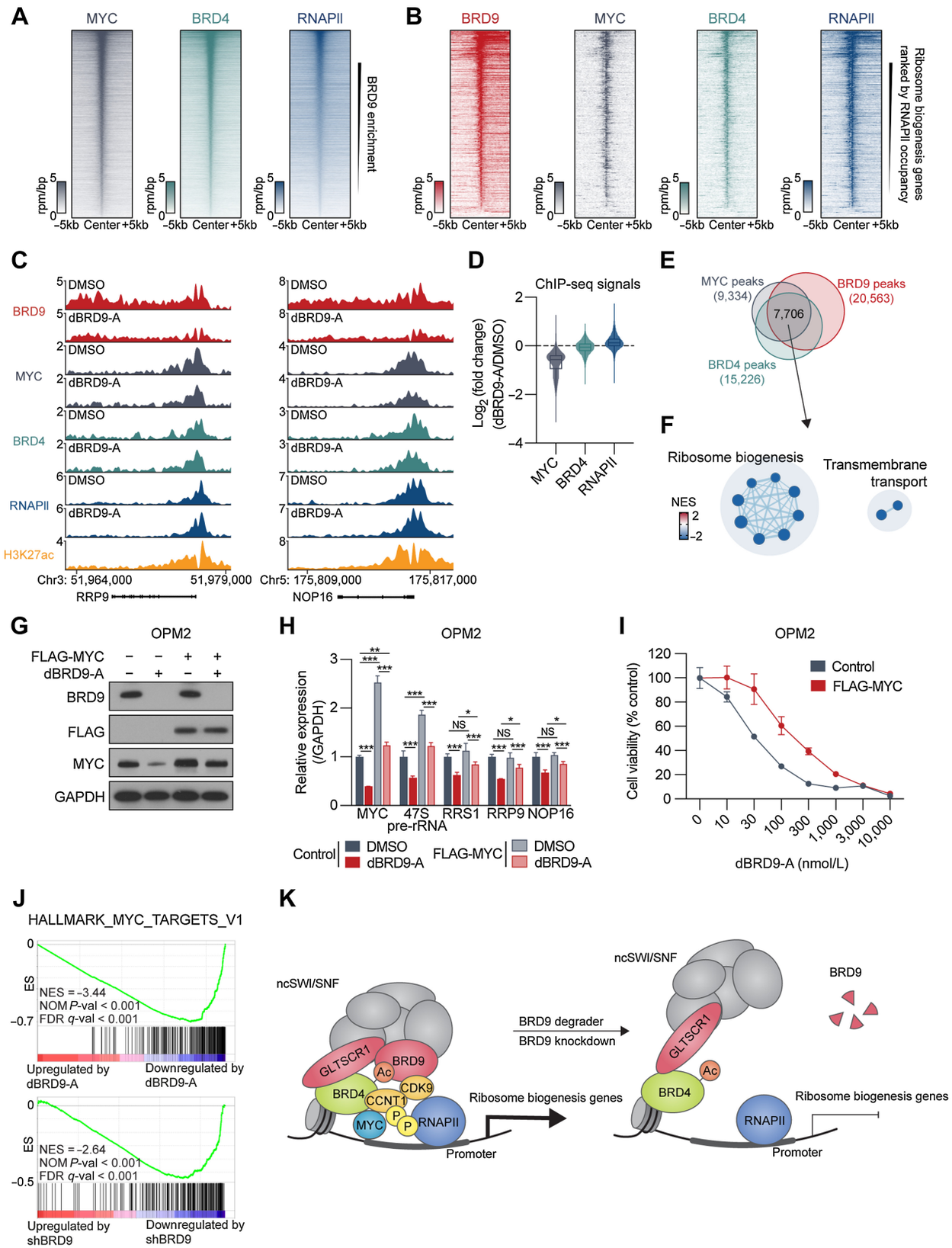

Discussion

Increased ribosome production and activity play a central role in promoting tumorigenesis in a broad spectrum of cancers (19–21, 27). Many DNA-damaging agents inhibit ribosome biogenesis, which supports ribosome biogenesis as a novel therapeutic target in cancer (27, 28, 58, 59). In particular, doxorubicin and bortezomib have been reported to inhibit rRNA transcription and late rRNA processing, respectively, suggesting that these are critical cellular mechanisms in MM (60). Importantly, inhibitors of ribosome biogenesis show promising results in clinical trials (27, 28), representing a potential therapeutic target in MM (26, 61, 62). In fact, here we show that ribosome biogenesis gene expression is correlated with a poor prognosis and is disrupted by BRD9 inhibition. BRD9 colocalized with BRD4 and MYC to form a transcription initiation complex at these genes. In MM, MYC is frequently dysregulated due to translocation or amplification (63–65) and regulates diverse cellular processes (63–65), notably functioning as a master regulator of ribosome biogenesis (57). Consistent with previous reports in other cancer models (13, 66, 67), we found that BRD9 depletion also downregulated MYC transcription. We also found that MYC and BRD9 share a significant portion of binding sites at the TSS of their target genes. These results suggest that BRD9 supports ribosome biogenesis in MM by promoting not only MYC expression, but also MYC transcriptional activity. In addition, our results are supported by a previous report showing that the BRD4-bromodomain is required for BRD9 localization to genomic targets (56). Interestingly, Sima and colleagues also reported that depletion of BRD9 alters the ribosomal pathway in several pooled cancer cell lines (68), suggesting that BRD9 plays a critical role in regulating ribosome biogenesis in a broad range of cancers.

We also showed that protein synthesis was reduced in MM cells as a result of the reduction in ribosome biogenesis caused by BRD9 depletion. Generally, inhibition of protein synthesis leads to a preferential depletion of short-lived proteins (69). Indeed, we observed that cell-cycle proteins such as CDK4, CDC25A, and CDC6, which are well-known short-lived proteins (69, 70), are decreased by BRD9 depletion. This is consistent with the result that dBRD9-A treatment causes G_1 cell-cycle arrest in MM cells, which may play a functional role in the anti-MM activity of BRD9 depletion.

BRD9 plays an oncogenic role in several cancer types (9–11, 13, 66, 67, 71, 72), and clinical trials using BRD9 degraders are ongoing for synovial sarcoma and SMARCB1-deleted solid tumors (73). A predominant determinant of BRD9 dependency in cancer cells are mutations or fusion events that lead to aberrant mSWI/SNF complex formation and global changes in chromatin occupancy (2–4, 9). In MM, Shain and colleagues reported a mutation frequency of 16% in members of the mSWI/SNF subunit (6), and we did not find a significant correlation between BRD9 dependency and mSWI/SNF mutations in MM cell lines. In fact, we demonstrated for the first time that the susceptibility of MM cell lines to BRD9 depletion is associated with activation of ribosome biogenesis, translation machinery, and MYC transcriptional activity. Previous findings have shown that, in MM cells harboring t(4;14), snoRNAs specifically target ribosome biogenesis (62), and MMSET product stimulates cell growth via microRNA-mediated modulation of MYC (74). However, in this study, there was no association between sensitivity to BRD9 depletion and genetic background, including t(4;14). Given the wide variation in sensitivity to BRD9 depletion in MM cell lines (although the limited number of patient samples were generally sensitive), subset selection may be necessary when targeting BRD9 in clinical applications. To conclude this question, a large-scale study using patient samples is warranted.

Recently, Weisberg and colleagues also reported that BRD9 is a potential therapeutic target for MM (17). They showed that BRD9 knockdown and a novel BRD9 degrader (QA-68) reduced cell viability and caused G_1 cell-cycle arrest *in vitro* using H929 and MM.1S cells. Interestingly, they also demonstrated that BRD9 degraders nicely synergize with pomalidomide in MM cells. Both dBRD9-A and QA-68 employ IMiDs (lenalidomide and pomalidomide) as cereblon-binding moieties, which theoretically competes with free IMiDs. Although a more careful investigation is needed, this synergistic effect is a promising observation in clinical applications. Proteasome inhibitors, which are another set of standard drugs for MM, also attenuate the effects of BRD9 degraders and hence are not suitable for studying combination effects, at least *in vitro*. In this study, we found synergistic effects of dBRD9-A with palbociclib, melphalan, and dexamethasone. In particular, the strong synergistic effect of dBRD9-A and dexamethasone observed in this study supports the finding that BRD9 restricts glucocorticoid receptor binding (47) and may propose a new therapeutic regimen for MM treatment.

In summary, our data identify a novel function for BRD9 in promoting ribosome biogenesis in MM and, conversely, demonstrate that BRD9 depletion impairs ncBAF localization to its genomic targets, thereby disrupting ribosome biogenesis machinery. Because overexpression of BRD9 and activated ribosome biogenesis play critical roles in driving MM tumorigenesis, our results provide the rationale for further evaluation of BRD9 degraders as novel treatments in MM.

Figure 6.

BRD9 colocalized with BRD4 and MYC in ribosome biogenesis gene promoters. **A,** Tornado plots showing BRD9 enrichment at regions bound by MYC, BRD4, and RNAPII ChIP-signal ± 5 kb in OPM2 cells. **B,** Tornado plots showing BRD9, MYC, BRD4, and RNAPII ChIP-signal ± 5 kb of ribosome biogenesis gene promoters in OPM2 cells. Promoters are ranked by RNAPII ChIP-signal. **C,** Representative gene tracks showing BRD9, MYC, BRD4, RNAPII, and H3K27Ac ChIP-seq occupancy at the indicated genomic loci in dBRD9-A or DMSO-treated OPM2 cells. **D,** Violin plot representing changes in MYC, BRD4, and RNAPII occupancy at each peak region in ChIP-Rx experiments of dBRD9-A (100 nmol/L)-treated OPM2 cells following a 24-hour treatment. **E,** Venn diagram overlaps of all identified BRD9 and BRD4 ChIP-seq peaks in OPM2 cells. **F,** GSEA of BRD9, MYC, and BRD4 overlapped genes for Gene Ontology (Biologic Process, MSigDB) summarized by a dot plot is shown. **G** and **H,** FLAG-tagged MYC or empty vector was overexpressed in OPM2 cells. Expression level of MYC measured by immunoblotting after treatment with or without dBRD9-A (100 nmol/L) for 24 hours (top, **G**). Expression level of indicated mRNAs was measured by qRT-PCR (**H**). **I,** FLAG-tagged MYC or empty vector overexpressed in OPM2 cells that were cultured with the indicated concentrations of dBRD9-A for 5 days. Viable cells were determined by MTT assay. Data represent mean ± SD of triplicate cultures. **J,** GSEA plots showed MYC target genes were downregulated by dBRD9-A (top) or shBRD9 (bottom). **K,** Proposed model of BRD9 (ncSWI/SNF) functions in MM cells. BRD9 binds to acetylated BRD4 and strengthens the interaction of ncBAF and BRD4, enhancing expression of ribosome biogenesis genes. Pharmacologic degradation or knockdown of BRD9 destabilizes the binding of ncSWI/SNF to BRD4 and reduces the transcription of the ribosome biogenesis genes.

Authors' Disclosures

J. Qi reports other support from Epiphanes and Talus outside the submitted work. K.C. Anderson reports personal fees from Pfizer, AstraZeneca, and Janssen, as well as other support from C4 Therapeutics, NextRNA, Window, and Starton during the conduct of the study. No disclosures were reported by the other authors.

Authors' Contributions

K. Kurata: Formal analysis, validation, investigation, visualization, methodology, writing–original draft. **M.K. Samur:** Data curation, formal analysis. **P. Liow:** Resources, investigation. **K. Wen:** Investigation. **L. Yamamoto:** Investigation. **J. Liu:** Investigation. **E. Morelli:** Investigation. **A. Gulla:** Investigation. **Y.T. Tai:** Resources. **J. Qi:** Resources. **T. Hideshima:** Conceptualization, formal analysis, supervision, funding acquisition, investigation, methodology, writing–review and editing. **K.C. Anderson:** Conceptualization, supervision, funding acquisition, project administration, writing–review and editing.

Acknowledgments

The authors thank the Molecular Biology Core Facilities, Dana-Farber Cancer Institute for assistance with RNA-seq and Chip-seq analysis; the Animal Resources Facility, Dana-Farber Cancer Institute for support with animal studies. This work was supported by the Stuchin Family Fellowship (to K. Kurata), the Vicki and Neal Roth Fellowship for Multiple Myeloma Research (to K. Kurata), the Brian D. Novis Junior Grant from the International Myeloma Foundation (to E. Morelli), the Career Enhancement Award from Dana Farber/Harvard Cancer Center SPORE in Multiple Myeloma (SPORE-P50CA100707; to E. Morelli), the Special Fellow grant from The Leukemia & Lymphoma Society (to E. Morelli), the Fellow-to-Faculty Scholar Award from the American Society of Hematology (to E. Morelli), the Individual Start-UP grant from the Italian Association for Cancer Research (project #27750; to A. Gulla), NIH grant 5P50CA100707 (to K.C. Anderson), R01-CA050947 (to K.C. Anderson), R01-CA178264 (to T. Hideshima, K.C. Anderson), P01–155258 (to K.C. Anderson), R01CA233601 (to J. Qi), the Adelson Medical Research Foundation and the Paula and Rodger Riney Foundation (to K.C. Anderson), and a Leukemia & Lymphoma Society TRP grant (to J. Qi). A. Gulla is a fellow of the Leukemia and Lymphoma Society and a Scholar of the American Society of Hematology. K.C. Anderson is an American Cancer Society Clinical Research Professor.

The publication costs of this article were defrayed in part by the payment of publication fees. Therefore, and solely to indicate this fact, this article is hereby marked "advertisement" in accordance with 18 USC section 1734.

Note

Supplementary data for this article are available at Clinical Cancer Research Online (http://clincancerres.aacrjournals.org/).

Received November 25, 2022; revised January 12, 2023; accepted February 9, 2023; published first February 13, 2023.

References

1. Narlikar GJ, Sundaramoorthy R, Owen-Hughes T. Mechanisms and functions of ATP-dependent chromatin-remodeling enzymes. Cell 2013;154:490–503.
2. Centore RC, Sandoval GJ, Soares LMM, Kadoch C, Chan HM. Mammalian SWI/SNF chromatin remodeling complexes: emerging mechanisms and therapeutic strategies. Trends Genet 2020;36:936–50.
3. Mittal P, Roberts CWM. The SWI/SNF complex in cancer—biology, biomarkers and therapy. Nat Rev Clin Oncol 2020;17:435–48.
4. Hohmann AF, Vakoc CR. A rationale to target the SWI/SNF complex for cancer therapy. Trends Genet 2014;30:356–63.
5. Kadoch C, Hargreaves DC, Hodges C, Elias L, Ho L, Ranish J, et al. Proteomic and bioinformatic analysis of mammalian SWI/SNF complexes identifies extensive roles in human malignancy. Nat Genet 2013;45:592–601.
6. Shain AH, Pollack JR. The spectrum of SWI/SNF mutations, ubiquitous in human cancers. PLoS One 2013;8:e55119.
7. Pan J, Meyers RM, Michel BC, Mashtalir N, Sizemore AE, Wells JN, et al. Interrogation of mammalian protein complex structure, function, and membership using genome-scale fitness screens. Cell Syst 2018;6:555–68.
8. Mashtalir N, D'Avino AR, Michel BC, Luo J, Pan J, Otto JE, et al. Modular organization and assembly of SWI/SNF family chromatin remodeling complexes. Cell 2018;175:1272–88.
9. Zhu X, Liao Y, Tang L. Targeting BRD9 for cancer treatment: a new strategy. Onco Targets Ther 2020;13:13191–200.
10. Wang X, Wang S, Troisi EC, Howard TP, Haswell JR, Wolf BK, et al. BRD9 defines a SWI/SNF sub-complex and constitutes a specific vulnerability in malignant rhabdoid tumors. Nat Commun 2019;10:1881.
11. Brien GL, Remillard D, Shi J, Hemming ML, Chabon J, Wynne K, et al. Targeted degradation of BRD9 reverses oncogenic gene expression in synovial sarcoma. Elife 2018;7:e41305.
12. McBride MJ, Pulice JL, Beird HC, Ingram DR, D'Avino AR, Shern JF, et al. The SS18-SSX fusion oncoprotein hijacks BAF complex targeting and function to drive synovial sarcoma. Cancer Cell 2018;33:1128–41.
13. Hohmann AF, Martin LJ, Minder JL, Roe JS, Shi J, Steurer S, et al. Sensitivity and engineered resistance of myeloid leukemia cells to BRD9 inhibition. Nat Chem Biol 2016;12:672–9.
14. Alpsoy A, Utturkar SM, Carter BC, Dhiman A, Torregrosa-Allen SE, Currie MP, et al. BRD9 is a critical regulator of androgen receptor signaling and prostate cancer progression. Cancer Res 2021;81:820–33.
15. Lou W, Gao K, Xu C, Li Q. Bromodomain-containing protein 9 is a prognostic biomarker associated with immune infiltrates and promotes tumor malignancy through activating notch signaling pathway in negative HIF-2α clear cell renal cell carcinoma. IUBMB Life 2021;73:1334–47.
16. Mason LD, Chava S, Reddi KK, Gupta R. The BRD9/7 inhibitor TP-472 blocks melanoma tumor growth by suppressing ECM-mediated oncogenic signaling and inducing apoptosis. Cancers (Basel) 2021;13:5516.
17. Weisberg E, Chowdhury B, Meng C, Case AE, Ni W, Garg S, et al. BRD9 degraders as chemosensitizers in acute leukemia and multiple myeloma. Blood Cancer J 2022;12:110.
18. Orsolic I, Jurada D, Pullen N, Oren M, Eliopoulos AG, Volarevic S. The relationship between the nucleolus and cancer: current evidence and emerging paradigms. Semin Cancer Biol 2016;37–38:36–50.
19. Truitt ML, Ruggero D. New frontiers in translational control of the cancer genome. Nat Rev Cancer 2016;16:288–304.
20. Bhat M, Robichaud N, Hulea L, Sonenberg N, Pelletier J, Topisirovic I. Targeting the translation machinery in cancer. Nat Rev Drug Discov 2015;14:261–78.
21. Truitt ML, Conn CS, Shi Z, Pang X, Tokuyasu T, Coady AM, et al. Differential requirements for eIF4E dose in normal development and cancer. Cell 2015;162:59–71.
22. Vogel C, Marcotte EM. Insights into the regulation of protein abundance from proteomic and transcriptomic analyses. Nat Rev Genet 2012;13:227–32.
23. Bruno PM, Liu Y, Park GY, Murai J, Koch CE, Eisen TJ, et al. A subset of platinum-containing chemotherapeutic agents kills cells by inducing ribosome biogenesis stress. Nat Med 2017;23:461–71.
24. Bywater MJ, Poortinga G, Sanij E, Hein N, Peck A, Cullinane C, et al. Inhibition of RNA polymerase I as a therapeutic strategy to promote cancer-specific activation of p53. Cancer Cell 2012;22:51–65.
25. Drygin D, Siddiqui-Jain A, O'Brien S, Schwaebe M, Lin A, Bliesath J, et al. Anticancer activity of CX-3543: a direct inhibitor of rRNA biogenesis. Cancer Res 2009;69:7653–61.
26. Manier S, Huynh D, Shen YJ, Zhou J, Yusufzai T, Salem KZ, et al. Inhibiting the oncogenic translation program is an effective therapeutic strategy in multiple myeloma. Sci Transl Med 2017;9:eaal2668.
27. Pelletier J, Thomas G, Volarević S. Ribosome biogenesis in cancer: new players and therapeutic avenues. Nat Rev Cancer 2018;18:51–63.
28. Catez F, Dalla Venezia N, Marcel V, Zorbas C, Lafontaine DLJ, Diaz JJ. Ribosome biogenesis: an emerging druggable pathway for cancer therapeutics. Biochem Pharmacol 2019;159:74–81.
29. Kumar SK, Rajkumar V, Kyle RA, van Duin M, Sonneveld P, Mateos MV, et al. Multiple myeloma. Nat Rev Dis Primers 2017;3:17046.
30. Ohguchi H, Park PMC, Wang T, Gryder BE, Ogiya D, Kurata K, et al. Lysine demethylase 5A is required for MYC driven transcription in multiple myeloma. Blood Cancer Discov 2021;2:370–87.
31. Morita M, Alain T, Topisirovic I, Sonenberg N. Polysome profiling analysis. Bio-protocol 2013;3:e833.

32. Chauhan D, Tian Z, Nicholson B, Kumar KG, Zhou B, Carrasco R, et al. A small molecule inhibitor of ubiquitin-specific protease-7 induces apoptosis in multiple myeloma cells and overcomes bortezomib resistance. Cancer Cell 2012;22:345–58.
33. Chng WJ, Kumar S, Vanwier S, Ahmann G, Price-Troska T, Henderson K, et al. Molecular dissection of hyperdiploid multiple myeloma by gene expression profiling. Cancer Res 2007;67:2982–9.
34. Samur MK, Minvielle S, Gulla A, Fulciniti M, Cleynen A, Aktas Samur A, et al. Long intergenic non-coding RNAs have an independent impact on survival in multiple myeloma. Leukemia 2018;32:2626–35.
35. Attal M, Lauwers-Cances V, Hulin C, Leleu X, Caillot D, Escoffre M, et al. Lenalidomide, bortezomib, and dexamethasone with transplantation for myeloma. N Engl J Med 2017;376:1311–20.
36. Rooney MS, Shukla SA, Wu CJ, Getz G, Hacohen N. Molecular and genetic properties of tumors associated with local immune cytolytic activity. Cell 2015;160:48–61.
37. Trerè D. AgNOR staining and quantification. Micron 2000;31:127–31.
38. Lerdrup M, Johansen JV, Agrawal-Singh S, Hansen K. An interactive environment for agile analysis and visualization of ChIP-sequencing data. Nat Struct Mol Biol 2016;23:349–57.
39. Tsherniak A, Vazquez F, Montgomery PG, Weir BA, Kryukov G, Cowley GS, et al. Defining a cancer dependency map. Cell 2017;170:564–76.
40. Mitsiades CS, Mitsiades N, Poulaki V, Schlossman R, Akiyama M, Chauhan D, et al. Activation of NF-kappaB and upregulation of intracellular anti-apoptotic proteins via the IGF-1/Akt signaling in human multiple myeloma cells: therapeutic implications. Oncogene 2002;21:5673–83.
41. Mitsiades CS, Mitsiades NS, Richardson PG, Munshi NC, Anderson KC. Multiple myeloma: a prototypic disease model for the characterization and therapeutic targeting of interactions between tumor cells and their local microenvironment. J Cell Biochem 2007;101:950–68.
42. Remillard D, Buckley DL, Paulk J, Brien GL, Sonnett M, Seo HS, et al. Degradation of the BAF complex factor BRD9 by heterobifunctional ligands. Angew Chem Int Ed Engl 2017;56:5738–43.
43. Békés M, Langley DR, Crews CM. PROTAC targeted protein degraders: the past is prologue. Nat Rev Drug Discov 2022;21:181–200
44. George DE, Tepe JJ. Advances in proteasome enhancement by small molecules. Biomolecules 2021;11:1789.
45. Leestemaker Y, de Jong A, Witting KF, Penning R, Schuurman K, Rodenko B, et al. Proteasome activation by small molecules. Cell Chem Biol 2017;24:725–36.
46. Miettinen TP, Peltier J, Härtlova A, Gierliński M, Jansen VM, Trost M, et al. Thermal proteome profiling of breast cancer cells reveals proteasomal activation by CDK4/6 inhibitor palbociclib. Embo J 2018;37:e98359.
47. Wang L, Oh TG, Magida J, Estepa G, Obayomi SMB, Chong LW, et al. Bromodomain containing 9 (BRD9) regulates macrophage inflammatory responses by potentiating glucocorticoid receptor activity. Proc Natl Acad Sci U S A 2021;118:e2109517118.
48. Tessoulin B, Moreau-Aubry A, Descamps G, Gomez-Bougie P, Maïga S, Gaignard A, et al. Whole-exon sequencing of human myeloma cell lines shows mutations related to myeloma patients at relapse with major hits in the DNA regulation and repair pathways. J Hematol Oncol 2018;11:137.
49. Kanehisa M, Goto S. KEGG: Kyoto encyclopedia of genes and genomes. Nucleic Acids Res 2000;28:27–30.
50. Croft D, O'Kelly G, Wu G, Haw R, Gillespie M, Matthews L, et al. Reactome: a database of reactions, pathways and biological processes. Nucleic Acids Res 2011;39:D691–7.
51. Huang da W, Sherman BT, Lempicki RA. Bioinformatics enrichment tools: paths toward the comprehensive functional analysis of large gene lists. Nucleic Acids Res 2009;37:1–13.
52. Huang da W, Sherman BT, Lempicki RA. Systematic and integrative analysis of large gene lists using DAVID bioinformatics resources. Nat Protoc 2009;4:44–57.
53. Rahman S, Sowa ME, Ottinger M, Smith JA, Shi Y, Harper JW, et al. The Brd4 extraterminal domain confers transcription activation independent of pTEFb by recruiting multiple proteins, including NSD3. Mol Cell Biol 2011;31:2641–52.
54. Han F, Zhang L, Chen C, Wang Y, Zhang Y, Qian L, et al. GLTSCR1 negatively regulates BRD4-dependent transcription elongation and inhibits CRC metastasis. Adv Sci (Weinh) 2019;6:1901114.
55. Alpsoy A, Dykhuizen EC. Glioma tumor suppressor candidate region gene 1 (GLTSCR1) and its paralog GLTSCR1-like form SWI/SNF chromatin remodeling subcomplexes. J Biol Chem 2018;293:3892–903.
56. Gatchalian J, Malik S, Ho J, Lee DS, Kelso TWR, Shokhirev MN, et al. A non-canonical BRD9-containing BAF chromatin remodeling complex regulates naive pluripotency in mouse embryonic stem cells. Nat Commun 2018;9:5139.
57. Destefanis F, Manara V, Bellosta P. Myc as a regulator of ribosome biogenesis and cell competition: a link to cancer. Int J Mol Sci 2020;21:4037.
58. Golomb L, Volarevic S, Oren M. p53 and ribosome biogenesis stress: the essentials. FEBS Lett 2014;588:2571–9.
59. Woods SJ, Hannan KM, Pearson RB, Hannan RD. The nucleolus as a fundamental regulator of the p53 response and a new target for cancer therapy. Biochim Biophys Acta 2015;1849:821–9.
60. Burger K, Mühl B, Harasim T, Rohrmoser M, Malamoussi A, Orban M, et al. Chemotherapeutic drugs inhibit ribosome biogenesis at various levels. J Biol Chem 2010;285:12416–25.
61. Lee HC, Wang H, Baladandayuthapani V, Lin H, He J, Jones RJ, et al. RNA polymerase I inhibition with CX-5461 as a novel therapeutic strategy to target MYC in multiple myeloma. Br J Haematol 2017;177:80–94.
62. Oliveira V, Mahajan N, Bates ML, Tripathi C, Kim KQ, Zaher HS, et al. The snoRNA target of t(4;14) in multiple myeloma regulates ribosome biogenesis. FASEB Bioadv 2019;1:404–14.
63. Dang CV. MYC on the path to cancer. Cell 2012;149:22–35.
64. Stine ZE, Walton ZE, Altman BJ, Hsieh AL, Dang CV. MYC, metabolism, and cancer. Cancer Discov 2015;5:1024–39.
65. Jovanović KK, Roche-Lestienne C, Ghobrial IM, Facon T, Quesnel B, Manier S. Targeting MYC in multiple myeloma. Leukemia 2018;32:1295–306.
66. Bevill SM, Olivares-Quintero JF, Sciaky N, Golitz BT, Singh D, Beltran AS, et al. GSK2801, a BAZ2/BRD9 bromodomain inhibitor, synergizes with BET inhibitors to induce apoptosis in triple-negative breast cancer. Mol Cancer Res 2019;17:1503–18.
67. Bell CM, Raffeiner P, Hart JR, Vogt PK. PIK3CA cooperates with KRAS to promote MYC activity and tumorigenesis via the bromodomain protein BRD9. Cancers (Basel) 2019;11:1634.
68. Sima X, He J, Peng J, Xu Y, Zhang F, Deng L. The genetic alteration spectrum of the SWI/SNF complex: the oncogenic roles of BRD9 and ACTL6A. PLoS One 2019;14:e0222305.
69. Li J, Cai Z, Vaites LP, Shen N, Mitchell DC, Huttlin EL, et al. Proteome-wide mapping of short-lived proteins in human cells. Mol Cell 2021;81:4722–35.
70. Teixeira LK, Reed SI. Ubiquitin ligases and cell cycle control. Annu Rev Biochem 2013;82:387–414.
71. Krämer KF, Moreno N, Frühwald MC, Kerl K. BRD9 inhibition, alone or in combination with cytostatic compounds as a therapeutic approach in rhabdoid tumors. Int J Mol Sci 2017;18:1537.
72. Del Gaudio N, Di Costanzo A, Liu NQ, Conte L, Migliaccio A, Vermeulen M, et al. BRD9 binds cell type-specific chromatin regions regulating leukemic cell survival via STAT5 inhibition. Cell Death Dis 2019;10:338.
73. Mullard A. Targeted protein degraders crowd into the clinic. Nat Rev Drug Discov 2021;20:247–50.
74. Mirabella F, Wu P, Wardell CP, Kaiser MF, Walker BA, Johnson DC, et al. MMSET is the key molecular target in t(4;14) myeloma. Blood Cancer J 2013;3:e114.